Front. Phys. 13(2), 134203 (2018)
https://doi.org/10.1007/s11467-017-0733-3

RESEARCH ARTICLE

Analysis of a conformal invisible device

Lin Xu[1,2], Zhan Xiong[2], Huan-Yang Chen[1,†]

[1] *Institute of Electromagnetics and Acoustics and Department of Electronic Science, Xiamen University, Xiamen 361005, China*
[2] *College of Physics, Optoelectronics and Energy, Soochow University, Suzhou 215006, China*
Corresponding author. E-mail: †kenyon@xmu.edu.cn
Received June 23, 2017; accepted September 12, 2017

We perform a semi-analytical calculation of the field distributions of a conformal invisible device via mode expansions. For a discrete set of frequencies in the regime of wave optics, the conformal invisible device is perfectly transparent, which stems from the special conformal mapping and the refractive-index profile of the Mikaelian lens.

Keywords conformal transformation optics, conformal invisible device, refractive-index profile

PACS numbers 42.25.Bs, 42.30.Va, 42.79.-e

1 Introduction

Optical invisibility was first revealed in transformation optics [1, 2]. In the last decade, various transformation optical devices have been proposed for manipulating the propagation of electromagnetic waves [3–6]. With the help of metamaterial development, some reduced experiments have been implemented, such as invisible cloaks [7], carpet cloaks [8–13], field rotators [14, 15], and concentrators [16, 17]. Transformation media from coordinate transformations between virtual space and physical space are usually inhomogeneous and anisotropic in three dimensional spaces [18, 19]. In two dimensions (2D), the relationship between physical space and virtual space may be established by conformal mappings [1, 20]. Because of the analytical condition of conformal mappings, transformation media are isotropic with a refractive-index profile [1, 20, 21], which eases experimental fabrications.

As a branch of transformation optics, conformal transformation optics [20] provides a simpler method to control light rays. A conformal invisible device was originally introduced for light rays other than waves [1]. Through the analogy between the Helmholtz equation and the stationary Schrödinger equation, it was found that conformal invisible devices can also work for optical waves with discrete frequencies [22], which enriched their applications [20]. In a previous study [1], a conformal invisible device had mismatched impedance along a circle, which is the image of a branch cut in virtual space by Zhukowski conformal mapping. Therefore, it is difficult to investigate analytical solutions of field distributions [7]. Recently, by elaborately tuning the parameters of a logarithmic conformal mapping and a truncated Mikaelian lens, a conformal cloak was designed for all directions in 2D, with impedance matching everywhere [23]. Moreover, the required refractive-index profile is further optimized, ranging from 0 to 5.127, which further enables its experimental realization.

In this study, we perform a semi-analytical calculation of the field distributions of a conformal invisible device by using mode analysis [23]. Owing to the structure of conformal mapping and the special refractive-index profile of the Mikaelian lens, we demonstrate that the conformal invisible device can work both for the geometric limit and the wave regime at eigenfrequencies.

2 Conformal invisible device

By introducing multi-value Riemann surfaces, conformal mappings can achieve one-to-one correspondence between a physical space and a virtual space [24]. Let us consider a conformal mapping with a linear term and dual logarithmic terms [23, 25], which is written as

$$w(z) = z + \alpha(\log(z-\beta) - \log(z+\beta)), \tag{1}$$

where α and β are two parameters to be determined. The domain (z complex plane) and range (w complex plane), i.e., the physical space and virtual space, are detailed in Appendix A. To investigate the propagation of electro-

magnetic waves in both spaces, the refractive-index profiles $n(z)$ and $n'(w)$ are introduced to the physical space and virtual space, respectively. Both spaces are treated as planar dielectric media with two-dimensional graded refractive-index profiles. They have continuous parallel symmetry on the third space dimension. In this paper, we only consider electromagnetic waves of transverse electric modes, with the electric field along the third dimension. The electric-field component in the physical space is governed by the Helmholtz equation [1, 20, 22],

$$[4\partial_z^*\partial_z + n^2(z)k^2]E(z) = 0, \tag{2}$$

where E is the electric field perpendicular to the z complex plane, $z = x + iy$, and k is the wave vector in free space. In the virtual space, the electric field also obeys the Helmholtz wave equation

$$[4\partial_w^*\partial_w + n'^2(w)k^2]E'(w) = 0, \tag{3}$$

where E' is the electric field perpendicular to the w complex plane with $w = u + \mathrm{i}v$.

For introducing the conformal mapping of Eq. (1) to connect the virtual space and physical space, we require the refractive-index profiles of both spaces satisfy the following equation [20]:

$$n(z) = n'(w)|\mathrm{d}w/\mathrm{d}z|. \tag{4}$$

We then map the Helmholtz equation of Eq. (2) to Eq. (3), i.e., $E(z) = E'(z(w))$, which means that light propagation in the physical space corresponds to that in the virtual space. That is, the form of the Helmholtz equation is invariant under conformal mapping [1] when Eq. (4) is satisfied.

In the following parts, we set $\alpha = 4$ and $\beta = 1.2$ for discussions (we use an arbitrary unit of length).

2.1 Geometric limit

In the limit of geometrical optics [19], light trajectories are connected between the physical space and virtual space because optical lengths are conserved under the conformal mapping of Eqs. (1) and (4) [20]. Therefore, if we can investigate the light propagation in one space, the light trajectory of another space can be derived simply via point-to-point mapping with Eq. (1). Let us consider a conformal invisible device with Eq. (1) [23]. Its virtual space is shown in Fig. 1(a). The upper sheet is endowed with a truncated Mikaelian lens, whose refractive-index profile is written as $1/\cosh(u/4)$. At the branch cut (line in black), the refractive index is unity. The refractive-index profile in the lower sheet is unity as well. The length of the branch cut is 12.077. Some parallel light rays (red lines with arrows) impinge the branch cut with

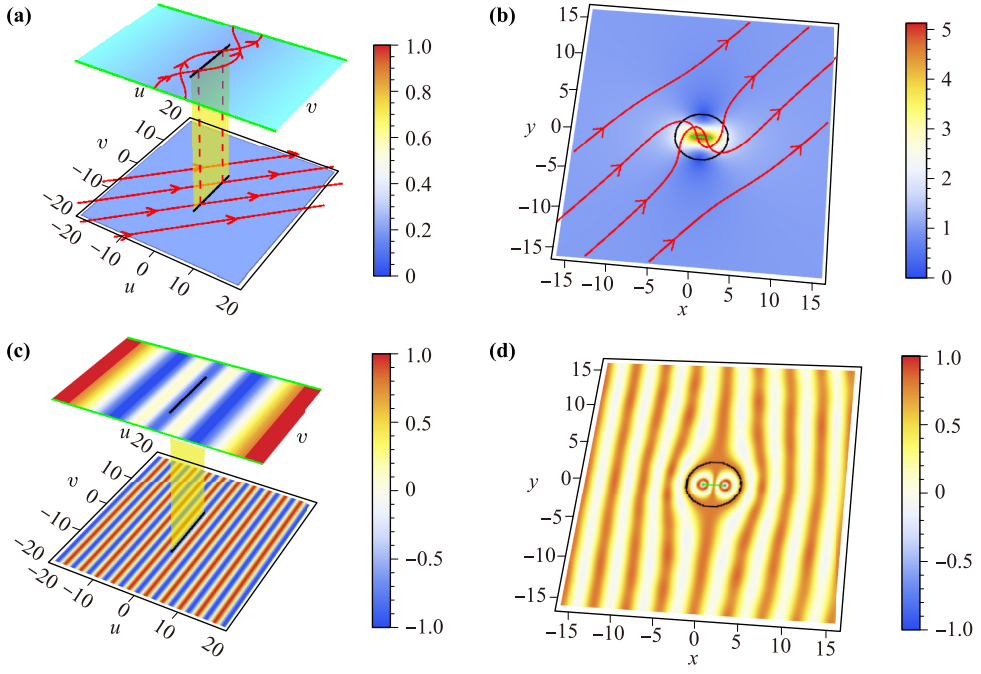

Fig. 1 Geometric optics and wave behavior in the virtual space and physical space of conformal invisible device. **(a)** Light rays in the virtual space. The lower sheet is uniform with a refractive index of unity, and the upper sheet is endowed with a truncated Mikaelian lens. **(b)** Light rays in the physical space. **(c)** Reduced wave solution in the virtual space, where $l = 4$. **(d)** Electric field in the physical space. In (a) and (b), the color bar represents the refractive-index profile, whereas in (c) and (d), the color bar denotes the real part of the electric field. In the virtual space, the green lines represent the periodicity of the upper sheet, and the black lines represent the branch cuts. Their images in the physical space are marked with corresponding colors.

an incident angle and enter the upper sheet without any reflection, which is bended to form closed curves via the Mikaelian lens [26, 27]. Therefore, if a light ray enters the upper sheet, it returns into the lower sheet after a closed curve. Together with those light rays not hitting the branch cut, they all continue their propagation as if nothing happened. A Mikaelian lens can be obtained from Maxwell's fisheye lens by employing optical exponential conformal mapping [28]. Via this mapping, we can obtain an analytical expression for light rays in the upper sheet using a simpler method [26, 27]. Light rays in the upper sheet are expressed as $\sinh u = \sin(v \pm 1.25)$.

As we can see, the range of the refractive-index profile in the virtual space is 0 to 1. After Eq. (1), the range of the transformed refractive-index profile is changed from 0 to 5.65, as shown in the contour plot of Fig. 1(b). Trajectories of light (red curves with arrows) in the physical space are mapped from those in the virtual space according to Eq. (1). One can also use the Euler–Lagrange equation from Fermat's principle or Hamilton's equation of optics to calculate the light trajectories in a physical space [19].

2.2 Wave regime

In the virtual space of the conformal invisible device, parallel light rays experience additional optical length if they impinge on the branch cut and enter the upper sheet, which can result in a phase delay. For human eyes, this phase delay could be usually ignored. However, a precise optical detection apparatus can easily sense this delay if parallel light pulses travel in the conformal invisible device. In the realm of wave optics, owing to this additional phase delay, the field pattern exhibits extreme interference, which usually results in the destruction of its invisible effect. However, when the phase delay is an integer multiple of 2π (heuristic understanding), we observe phase continuity along the branch cut, so that light waves propagate with a uniform wavefront in the steady-state and become invisible for waves.

Usually, it is difficult to obtain analytical results for the field distribution in space with a graded refractive-index profile [29]. Here, we perform a semi-analytical calculation to discuss the field distribution in the virtual space, as a simple treatment. In the lower sheet of Fig. 1(c), the solution should be a plane wave because of uniform refractive-index profile. The upper sheet has a period of 8π in the v direction. Together with the refractive-index profile, the upper sheet forms a cavity for the upper sheet. At the resonant frequencies of this cavity, the wavelength satisfies the following condition [26, 27]:

$$\lambda = 8\pi/\sqrt{l(l+1)}, \tag{5}$$

where $l \in N^+$. We will provide a detailed derivation in the next part. In the field distribution of Fig. 1(c), we choose $l = 4$. When a plane wave with this wavelength propagates in the lower sheet perpendicular to a branch cut, it excites an eigenmode of the upper sheet without breaking phase continuity along the branch cut. Fig. 1(d) shows numerical results for the field distribution in the physical space with the refractive-index profile in Fig. 1(b). We observe an almost perfect plane wavefront when a wave passes through the conformal invisible device.

2.3 Modes in upper sheet

As mentioned previously, the upper sheet of the virtual space is a truncated Mikaelian lens, and its field distribution is the critical to the invisibility of the whole device. Let us rewrite the Helmholtz equation [26, 27]:

$$\frac{\partial^2 E}{\partial u^2} + \frac{\partial^2 E}{\partial v^2} + k_0^2 \left(\frac{1}{\cosh(u/4)}\right)^2 E = 0. \tag{6}$$

Owing to the periodicity of 8π in the v direction, an electric field can be expressed as

$$E(w) = \psi(u)\mathrm{e}^{\mathrm{i}mv/(8\pi)}, \tag{7}$$

where $m \in N^+$. By introducing a new variable $\xi = \tanh(u/4)$, Eq. (6) can be transformed into

$$(1-\xi^2)\frac{\partial^2 \psi}{\partial \xi^2} - 2\xi\frac{\partial \psi}{\partial \xi} + \left[l(l+1) - \frac{m^2}{1-\xi^2}\right]\psi = 0, \tag{8}$$

where l satisfies Eq. (5). It is evident that solution of Eq. (8) is the associated Legendre polynomial with exponential term. Thus, the electric field can be written as

$$E(w) = P_l^m(\tanh(u/4))\mathrm{e}^{\mathrm{i}mv/(8\pi)}, \tag{9}$$

where P_l^m is the associated Legendre polynomial, l is a positive integer, and $m = -l, -l+1 \ldots l-1, l$.

Figures 2(a)–(c) show the field distribution when $l = 1$ and m equals -1, 0, and 1, respectively. Via the conformal mapping of Eq. (1), these fields can be mapped to the region in the physical space by changing variables:

$$E(z)=E(w(z))=P_l^m(\tanh(\mathrm{Re}(w(z))/4))\mathrm{e}^{\mathrm{i}m\mathrm{Im}(w(z))/(8\pi)}. \tag{10}$$

Figures 2(d)–(f) show the field distributions in the physical space corresponding to Figs. 2(a)–(c), respectively.

When $l \in N^+$, the field distribution has a stable pattern, which becomes the resonance conditions of the conformal invisible device for wave optics, which gives rise to Eq. (5). We also provide the field distributions of eigenmodes both in the virtual space and the physical space when $l = 2$; see Fig. A2 of Appendix B.

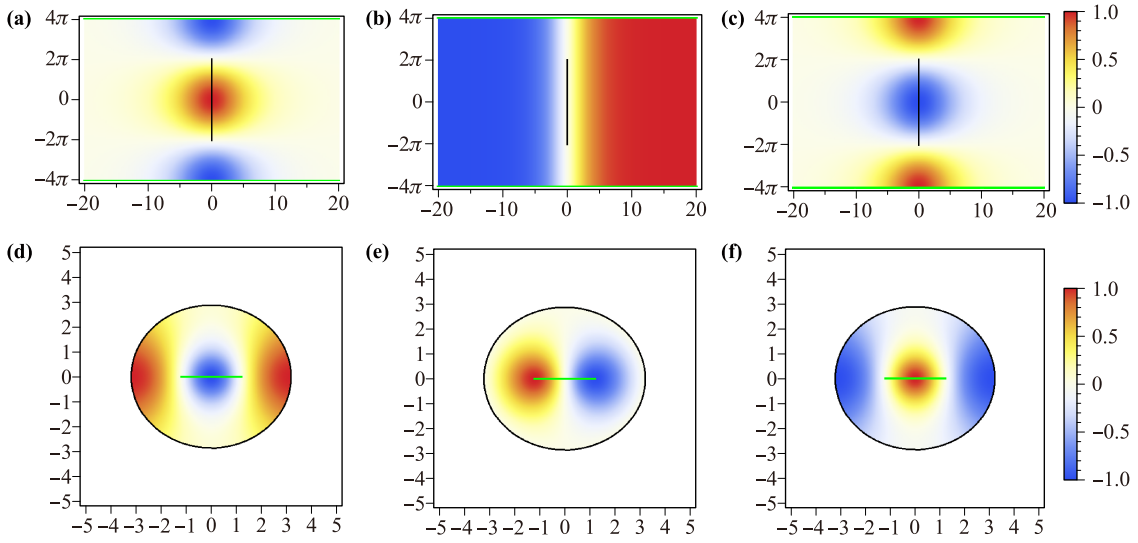

Fig. 2 Field distributions of eigenmodes in the virtual space with **(a)** $m = -1$, **(b)** $m = 0$, and **(c)** $m = 1$. Field distributions in the physical space with **(d)** $m = -1$, **(e)** $m = 0$, and **(f)** $m = 1$. In the virtual space, the green lines represent the periodicity of the upper sheet, and the black lines represent the branch cuts. Their images in the physical space are marked with corresponding colors.

2.4 Field in physical space

In the virtual space, light waves coming from different directions excite different modes of the upper sheet, which can be mapped to the physical space. The field distribution in the physical space at the resonant frequency is a linear combination of the mapped modes of the Mikaelian lens. The coefficients of these modes determine the field distribution of the Mikaelian lens. By tuning the magnitude and phase of the coefficients, we can achieve a field distribution that approximates that from numerical simulations. Figures 3(a)–(c) show three kinds of linear combination of mapped fields of the Mikaelian lens, with $l = 1$ in the physical space. The corresponding numerical simulations shown in Figs. 3(d)–(f) involve excitement by plane waves with incident angles of 0, $\pi/2$, and $\pi/4$,

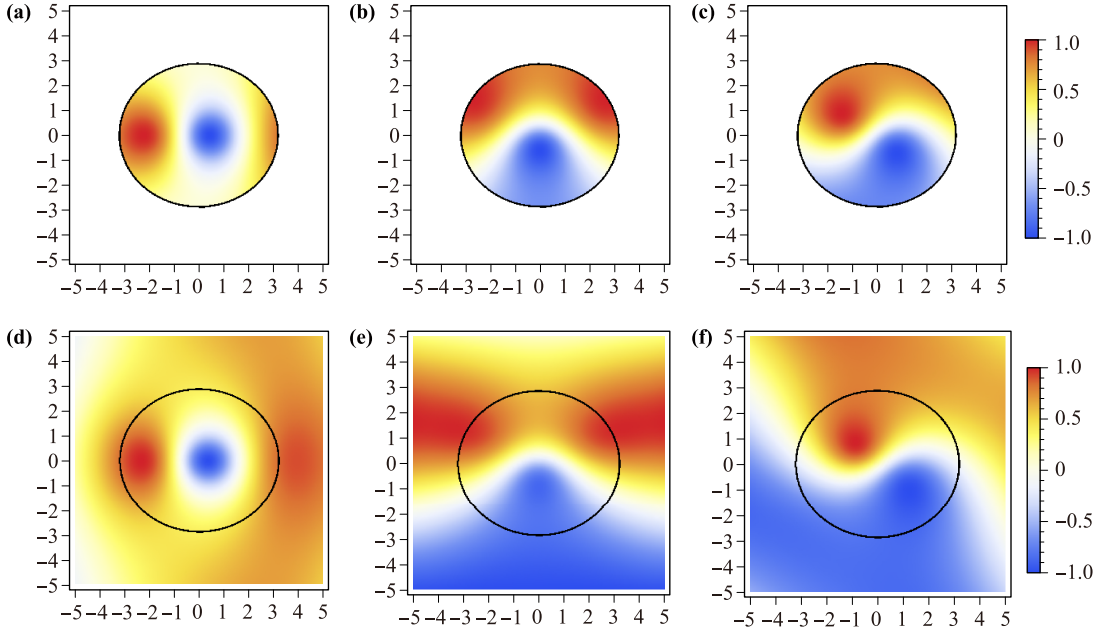

Fig. 3 Three kinds of linear combinations of eigenmodes with $l = 1$: **(a)**, **(b)**, and **(c)**. Corresponding numerical simulations of the field distributions in the physical space with incident angles of **(d)** 0, **(e)** $\pi/2$, and **(f)** $\pi/4$.

respectively. Regarding the region outside of the black closed curve, it is difficult to solve the field distribution analytically; thus, we use a numerical method to handle it. We also plot the distributions of the mapped field of the Mikaelian lens and their simulation results for $l = 2$ in Fig. A2 of Appendix B.

2.5 Invisibility effect

After clarifying the field distribution of the conformal invisible device under the resonant conditions of Eq. (5), we demonstrate an almost perfect invisibility effect with the field distributions shown in Fig. 4. Figures 3(a)–(c) show the center plots of Figs. 4(a)–(c). Figures 4(a)–(c) show that the plane wavefront is conserved when a light wave passes through the device with an incident angle of 0, $\pi/2$, or $\pi/4$, respectively. Figures 4(d)–(f) show the field distributions of the conformal invisible device at another frequency (l now taking a non-integer value of 1.5) with different incident angles. The plane wavefront is destroyed when a light wave travels across the device, which results in the disappearance of the invisibility effect. The invisibility effect is not perfect, because at a given resonant frequency with l, we only have $2l + 1$ mapped modes of the Mikaelian lens, which is a finite number. Therefore, we cannot find a superposition of these finite number of modes to have a specific field distribution along the branch cut such that the solution exactly matches a plane wave impinging on the branch cut at a given angle. In principle, if we have an infinite number of modes, we can achieve perfect matching. Thus, those modes can be combined to the corresponding plane wave distribution along the branch cut only approximately, which is why there is still slight deformation of the outgoing waves in Figs. 4(a)–(c).

The conformal invisible device can also hide a perfect electromagnetic conductor (PEC) [23] for light impinging from all angles. Figures 5(a)–(c) show the field distributions of a PEC (line in green) embedded in a conformal invisible device for plane waves incident with angles of 0, $\pi/2$, and $\pi/4$, respectively. The length of the PEC is 6.64472. The resonant frequency is chosen as $l = 6$. For comparison, Figs. 5(d)–(f) show the field distributions of a bare PEC for incident plane waves with angles of 0, $\pi/2$, and $\pi/4$, respectively. It can be seen that the bared PEC causes a shadow behind it. To create a cloaking region, we can further expand the PEC via other mappings [30].

To demonstrate the invisibility effect quantitatively, we calculate the far-field total scattering cross section σ in Fig. 6, corresponding to the normalized wavelength/α. For a bare PEC, the total scattering does not incur major deviation with wavelengths, as shown by the black curve. For a conformal invisible device and cloak with a PEC, the total scattering declines at resonant frequencies, as indicated by the green and red curves, respectively.

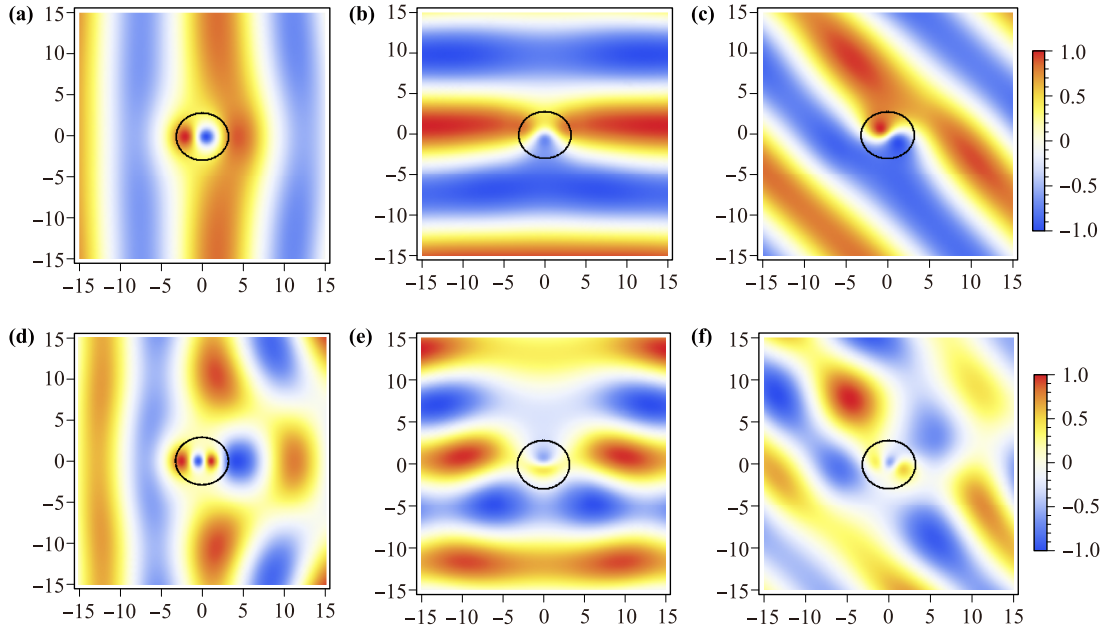

Fig. 4 Numerical simulations of the field distributions in the physical space of the conformal invisible device with incident angles of **(a)** 0, **(b)** $\pi/2$, and **(c)** $\pi/4$, where $l = 1$. For comparison, we plot the corresponding field distributions with incident angles of 0, $\pi/2$, and $\pi/4$ in **(d)**, **(e)**, and **(f)**, respectively, with $l = 1.5$.

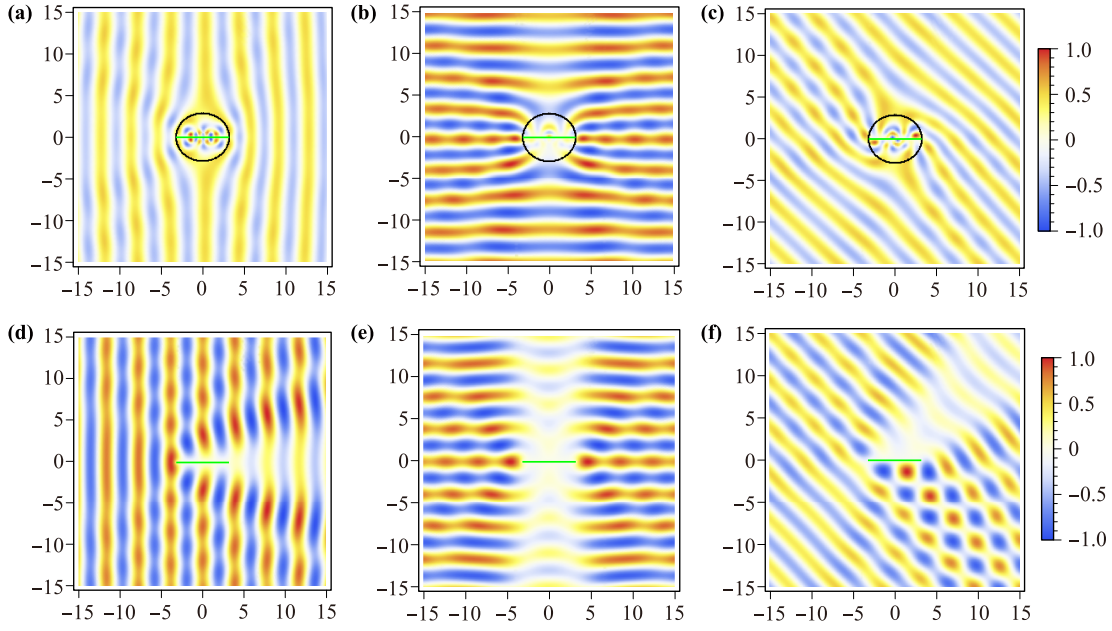

Fig. 5 Numerical simulations of the field distributions of a conformal invisible device with a PEC for incident angles of **(a)** 0, **(b)** $\pi/2$, and **(c)** $\pi/4$, where $l = 6$. For comparison, we plot the real part of the corresponding field distributions of a PEC for incident angles of 0, $\pi/2$, and $\pi/4$ in **(d)**, **(e)**, and **(f)**, respectively. The green lines denote the PEC.

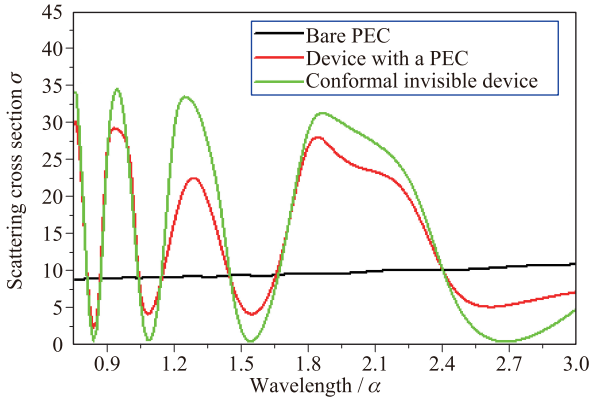

Fig. 6 Total scattering cross section σ changes with respect to the normalized wavelength/α for a bare PEC, the conformal invisible device, and the device with a PEC.

3 Conclusion

By using mode analysis, we perform semi-analytical calculations to demonstrate invisibility properties in a conformal device for wave optics discussed in Ref. [23]. The transparent effect of the conformal invisible device arises from the excitation of eigenmodes of the upper sheet of the virtual space, which results in phase continuity in the physical space. We show a heuristic physical picture of the conformal invisible device in the regimes of geometric optics and wave optics. This is helpful for optimizing the design and fabrication of conformal devices.

Appendix A The structure of the virtual and physical space of conformal mapping

Eq. (1), which is used for conformal mapping, comprises a linear term and dual logarithmic terms. Because of the multi-value property of logarithmic terms, we can rewrite Eq. (1) as

$$w(z) = z + \alpha \log\left|\frac{z-\beta}{z+\beta}\right| + \mathrm{i}\alpha\left[\arg\left(\frac{z-\beta}{z+\beta}\right) + 2m\pi\right], \tag{A1}$$

where m is an integer. To give its domain (physical space, z complex planes) and range (virtual space, w complex planes) a one-to-one correspondence, the virtual space and physical space are constructed as shown in Figs. A1(a) and (b), respectively. The virtual space is $m+1$ complex planes (in blue) connected with branch cuts (black lines). In Eq. (A1), "m" is an integer, and "1" is another whole complex plane, which can be divided into "m" slices by green lines. The regions marked by white numbers in the upper sheet and the complex planes marked with the same numbers are connected with branch cuts (line in black). In principle, m goes to infinity, which means that there are infinite complex planes. Here, we only plot five complex planes, for illus-

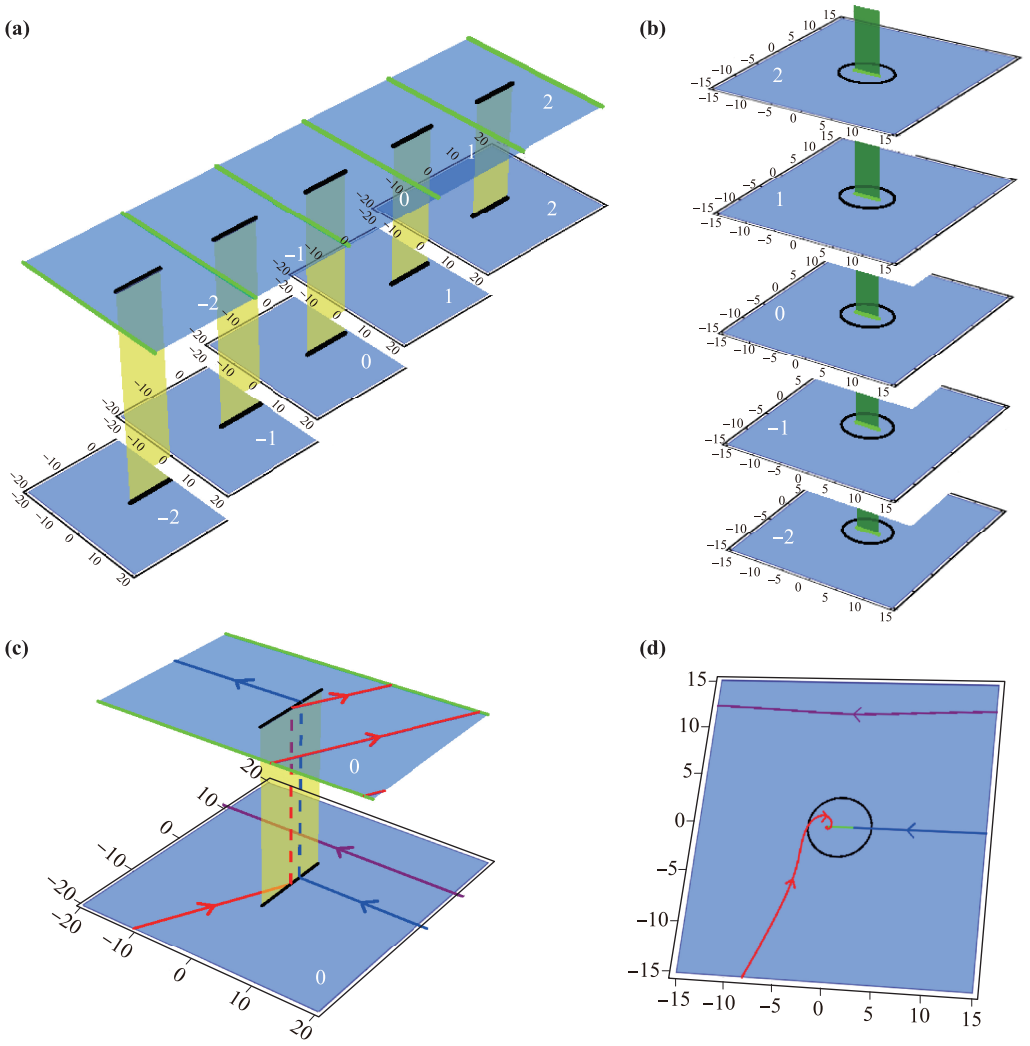

Fig. A1 Riemann surface of **(a)** the virtual space and **(b)** physical space, and effective structure of **(c)** virtual space and **(d)** physical space.

tration. To visualize the structure of the virtual space, an additional yellow slice is added to show the connection between the upper sheet and the corresponding lower ones. The physical space comprises m complex planes connected with branch cuts (green lines). Unlike the Riemann surface of exponential conformal mapping, a branch cut here is a line segment, not a ray (infinite in one direction). The black closed curves are mapped from the branch cuts of the virtual space. An additional green slice, which connects all the branch cuts in the physical space, is also introduced, for visualization. Now, we construct the Riemann surface of both the domain and range of Eq. (A1) to form a one-to-one correspondence. The effective structure of the physical space is a two-dimensional space described by one complex plane, which is marked with a white "0" in Fig. A1(d). The corresponding effective structure of the virtual space is a lower complex plane and an upper slice regionalso marked with a white "0," as shown in Fig. A1(c). In addition to branch cuts, light rays with blue, red, and purple lines with arrows are plotted in the virtual space. Their images (real trajectories) in the physical space are blue, red, and purple curves, respectively.

Appendix B Eigenmodes and their combinations for $l = 2$

For $l = 2$, the field distribution of eigenmodes in the virtual space are plotted in Figs. A2(a)–(e) for $m = -2, -1, 0, 1, 2$, respectively. The corresponding field distributions in the physical space are shown in Figs. A2(f)–(j) according to Eq. (10).

In the physical space, the field distribution at resonant

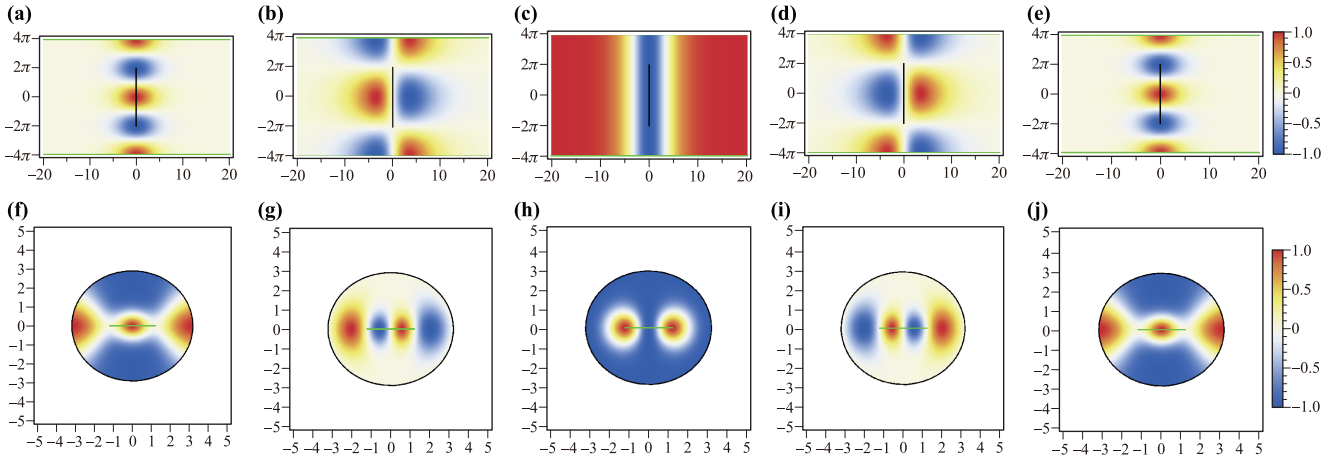

Fig. A2 Field distributions of eigenmodes in the virtual space with **(a)** $m = -2$, **(b)** $m = -1$, **(c)** $m = 0$, **(d)** $m = 1$, and **(e)** $m = 2$. Field distributions in the physical space with **(f)** $m = -2$, **(g)** $m = -1$, **(h)** $m = 0$, **(i)** $m = 1$, and **(j)** $m = 2$.

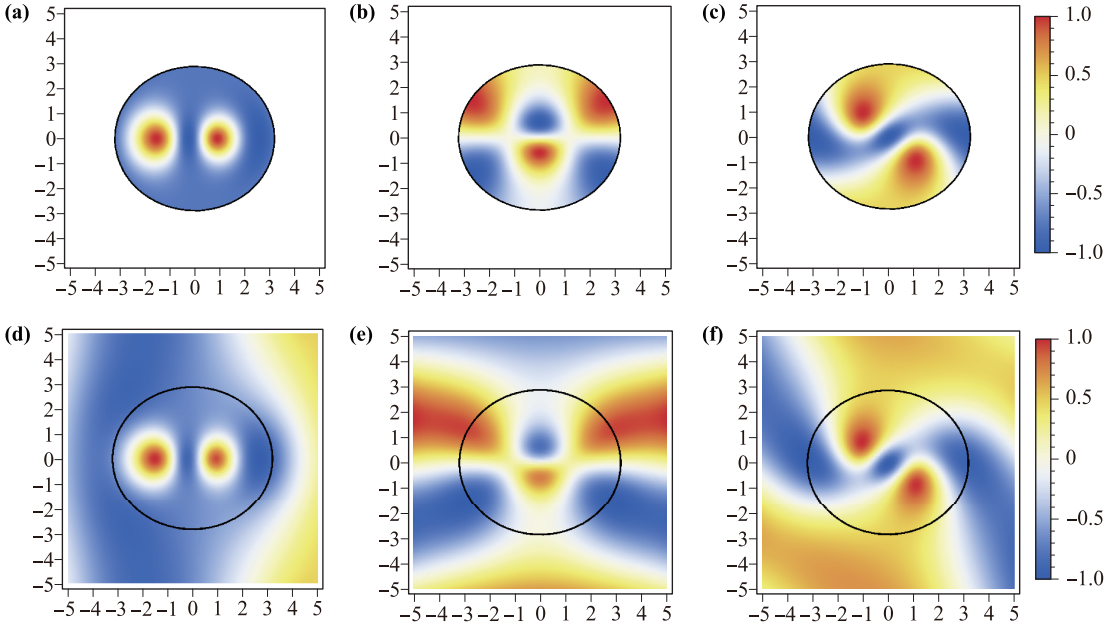

Fig. A3 Three kinds of linear combinations of eigenmodes: **(a)**, **(b)**, and **(c)**. Corresponding numerical field distributions in the physical space with incident angles of **(d)** 0, **(e)** $\pi/2$, and **(f)** $\pi/4$, respectively.

frequencies with $l = 2$ is the linear combination of eigenmodes of the Mikaelian lens shown in Figs. A2(f)–(j). Figures A3(a)–(c) show three kinds of linear combinations of eigenmodes for $l = 2$ in the physical space. Their corresponding numerical simulations in Figs. A3(d)–(f) involve excitement by plane waves with incident angles of 0, $\pi/2$, and $\pi/4$, respectively. The analytical solution and numerical results closely match.

Acknowledgements This work was supported by the National Natural Science Foundation of China for Excellent Young Scientists (Grant No. 61322504), the Foundation for the Author of National Excellent Doctoral Dissertation of China (Grant No. 201217), and Fundamental Research Funds for the Central Universities (Grant No. 20720170015).

References

1. U. Leonhardt, Optical conformal mapping, *Science* 312(5781), 1777 (2006)
2. J. B. Pendry, D. Schurig, and D. R. Smith, Controlling electromagnetic fields, *Science* 312(5781), 1780 (2006)
3. H. Y. Chen, C. T. Chan, and P. Sheng, Transformation optics and metamaterials, *Nat. Mater.* 9(5), 387 (2010)

4. A. V. Kildishev and V. M. Shalaev, Transformation optics and metamaterials, *Phys. Usp.* 54(1), 53 (2011)
5. Y. Liu and X. Zhang, Recent advances in transformation optics, *Nanoscale* 4(17), 5277 (2012)
6. P. Kinsler and M. W. McCall, The futures of transformations and metamaterials, *Photonics and Nanostructures – Fundamentals and Applications* 15, 10 (2015)
7. D. Schurig, J. J. Mock, B. J. Justice, S. A. Cummer, J. B. Pendry, A. F. Starr, and D. R. Smith, Metamaterial electromagnetic cloak at microwave frequencies, *Science* 314(5801), 977 (2006)
8. J. Li and J. B. Pendry, Hiding under the carpet: A new strategy for cloaking, *Phys. Rev. Lett.* 101(20), 203901 (2008)
9. R. Liu, C. Ji, J. J. Mock, J. Y. Chin, T. J. Cui, and D. R. Smith, Broadband ground-plane cloak, *Science* 323(5912), 366 (2009)
10. J. Valentine, J. Li, T. Zentgraf, G. Bartal, and X. Zhang, An optical cloak made of dielectrics, *Nat. Mater.* 8(7), 568 (2009)
11. L. H. Gabrielli, J. Cardenas, C. B. Poitras, and M. Lipson, Silicon nanostructure cloak operating at optical frequencies, *Nat. Photonics* 3(8), 461 (2009)
12. T. Ergin, N. Stenger, P. Brenner, J. B. Pendry, and M. Wegener, Three-dimensional invisibility cloak at optical wavelengths, *Science* 328(5976), 337 (2010)
13. H. F. Ma and T. J. Cui, Three-dimensional broadband ground-plane cloak made of metamaterials, *Nat. Commun.* 1(3), 1 (2010)
14. H. Y. Chen and C. T. Chan, Transformation media that rotate electromagnetic fields, *Appl. Phys. Lett.* 90(24), 241105 (2007)
15. H. Y. Chen, B. Hou, S. Chen, X. Ao, W. Wen, and C. T. Chan, Design and experimental realization of a broadband transformation media field rotator at microwave frequencies, *Phys. Rev. Lett.* 102(18), 183903 (2009)
16. M. Rahm, D. Schurig, D. A. Roberts, S. A. Cummer, D. R. Smith, and J. B. Pendry, Design of electromagnetic cloaks and concentrators using form-invariant coordinate transformations of Maxwell's equations, *Photonics and Nanostructures – Fundamentals and Applications* 6(1), 87 (2008)
17. M. M. Sadeghi, S. Li, L. Xu, B. Hou, and H. Y. Chen, Transformation optics with Fabry–Perot resonances, *Sci. Rep.* 5(1), 8680 (2015)
18. U. Leonhardt and T. G. Philbin, General relativity in electrical engineering, *New J. Phys.* 8(10), 247 (2006)
19. U. Leonhardt and T. Philbin, Geometry and Light: The Science of Invisibility, New York: Dover, Mineola, 2010
20. L. Xu and H. Y. Chen, Conformal transformation optics, *Nat. Photonics* 9(1), 15 (2014)
21. J. P. Turpin, A. T. Massoud, Z. H. Jiang, P. L. Werner, and D. H. Werner, Conformal mappings to achieve simple material parameters for transformation optics devices, *Opt. Express* 18(1), 244 (2010)
22. H. Y. Chen, U. Leonhardt, and T. Tyc, Conformal cloak for waves, *Phys. Rev. A* 83(5), 055801 (2011)
23. L. Xu, H. Y. Chen, T. Tyc, Y. Xie and S. A. Cummer, Perfect conformal invisible device with feasible refractive indexes, *Phys. Rev. B* 93, 041406(R) (2016)
24. Z. Nehari, Conformal Mapping, New York: McGraw-Hill, 1952
25. L. Xu and H. Y. Chen, Logarithm conformal mapping brings the cloaking effect, *Sci. Rep.* 4(1), 6862 (2015)
26. A. L. Mikaelian, The use of medium properties to focus waves, *Dokl. USSR Acad. Sci. Issue* 81, 569 (1951)
27. A. L. Mikaelian and A. M. Prokhorov, Self-focusing media with variable index of refraction, *Prog. Opt.* 17, 279 (1980)
28. T. Tyc, H. L. Dao, and A. J. Danner, Absolute optical instruments without spherical symmetry, *Phys. Rev. A* 92(5), 053827 (2015)
29. T. G. Philbin, Making geometrical optics exact, *J. Mod. Opt.* 61(7), 552 (2014)
30. H. Kan, L. Xu, Y. Xu, and H. Chen, Conformal cloaks from a function composition, *Europhys. Lett.* 117(3), 34002 (2017)